Research Square

Preprints are preliminary reports that have not undergone peer review.
They should not be considered conclusive, used to inform clinical practice,
or referenced by the media as validated information.

Investigating the Impact of Electric Micromobility Vehicle Fires in a Single-Level Passenger Railcar

Adam Barowy
UL Research Institutes
Charles Fleischmann
charley.fleischmann@ul.org
UL Research Institutes

Research Article

Keywords:

Posted Date: November 26th, 2026

DOI: https://doi.org/10.21203/rs.3.rs-11804783/v1

License: This work is licensed under a Creative Commons Attribution 4.0 International License.
Read Full License

Additional Declarations: No competing interests reported.

Investigating the Impact of Electric Micromobility Vehicle Fires in a Single-Level Passenger Railcar

Abstract

Passenger trains and subways are an attractive option for many commuters; however, station proximity is often too limited to be convenient. To address first/last mile travel needs, commuters are increasingly using electric micromobility vehicles (EMVs), including bringing personal EMVs onto public transport. This raises the question of the risk posed by an EMV fire in a passenger railcar.

In this study, three EMV types—a standing e-scooter, an e-bike, and a seated e-scooter—were forced into thermal runaway in a 72-passenger railcar to assess the hazard to passengers from an EMV fire. Tenability within the railcar was assessed using video observations, gas temperature, thermal radiation, and gas species measurements to evaluate visibility loss, asphyxiant fractional effective dose (FED), and thermal fractional effective dose (FED-T). The results quantify differences in tenability among devices stored in typical onboard locations and show that untenable conditions can develop throughout the railcar. Occupants in close proximity to the EMV, within a few rows, may be immediately threatened by the fireball resulting from ignition of the initial battery gas release.

Keywords: Train, thermal runaway, electric micromobility vehicle, lithium-ion battery, tenability

1 Introduction

The first/last mile (FLM) describes the distance a traveler must cover before boarding and/or after exiting a transport hub such as a train or bus station. For many travelers, FLM shapes perceptions of public transportation and can deter transit use [1]. For some travelers, micromobility vehicles are an attractive option and are an increasingly common solution to FLM travel. These vehicles span a wide range of device types and may be human-powered, electric, or hybrid. Common micromobility devices include bicycles, e-bikes, e-scooters, Segways, e-unicycles, and hoverboards. Reported benefits of micromobility include improved transportation accessibility, reduced traffic congestion, improved air quality, improved city sustainability, and lower accident rates [2]. This study focuses on electric micromobility vehicles (EMVs), including e-bikes and e-scooters, that use lithium-ion batteries for propulsion.

A practical challenge for EMVs is travel between stations on public transportation vehicles. In addition to storage limitations, there is a safety question: what risk is

posed to passengers if an EMV battery undergoes thermal runaway [3], leading to fire and/or explosion during transport?

Most modern EMVs rely on lithium-ion batteries (LiBs) to power an electric motor. LiBs offer high energy density, low maintenance, long service life, and fast charging. LiB-powered devices are widely used, often with little appreciation of the potential consequences of a LiB fire.

When a LiB fails and ignites, it is typically associated with thermal runaway. Thermal runaway occurs when exothermic reactions generate heat faster than it can be dissipated, leading to uncontrolled reaction rates. The most common causes attributed to thermal runaway are physical damage, overheating, and/or battery management system failure that results in overcharging, poor design and manufacturing defects. Failure mechanisms are commonly grouped into three categories: electrical, thermal, and mechanical abuse [4]. Electrical abuse [5] includes overcharge, over-discharge, and internal or external short circuit. Thermal abuse [6] includes overheating due to external heat exposure, including fire exposure [7]. Mechanical abuse [8] includes physical damage such as crushing or penetration [9].

The hazard posed by LiB thermal runaway in public transportation has been demonstrated by incidents involving consumer electronics, such as phones and laptops, overheating to the point of ignition. A notable case was the Samsung Galaxy Note 7, where battery defects led to a product recall [10]. Subsequent replacement issues resulted in the product being withdrawn from the market. In addition, the U.S. Department of Transportation, in coordination with the Federal Aviation Administration and the Pipeline and Hazardous Materials Safety Administration, issued an emergency order banning Samsung Galaxy Note 7 devices from aircraft in the United States [11].

Thermal runaway incidents involving EMVs in residential buildings have been reported in many cities worldwide [12–15], with particular scrutiny in New York City [16]. A recent UL Research Institute full-scale experimental study quantified hazards associated with seated e-scooter fires in residential settings [17]. In that study, thermal runaway was forced using electrical resistance heaters applied to five cells within the battery pack. Results showed that, in an unsprinklered home, seated e-scooter fires can become fatal within seconds. Occupants in close proximity may suffer fatal burns or succumb to smoke inhalation before escape, and additional occupants may be endangered if the e-scooter compromises the exit path.

Despite the growing prevalence of EMVs in multi-modal travel, experimental data describing the consequences of EMV battery thermal runaway within public transportation vehicles remain limited. Passenger railcars present a unique risk environment characterized by high occupant loads, relatively small compartment volumes, limited egress, few opportunities for rapid evacuation, and the typical absence of automatic fire suppression systems. In North America, fire safety regulations prioritize reducing the amount of combustibles in railcar construction, adding fire retardants to the remaining surface finish materials, and providing at least one portable fire extinguisher [18].

To address this gap, the paper reports provides the detailed experimental results from a series of full-scale fire experiments conducted in a passenger railcar common

across North America, in which three common EMV types—a standing e-scooter, an e-bike, and a seated e-scooter—were forced into thermal runaway. The experiments were designed to quantify fire development, thermal and toxic hazards, and passenger tenability associated with EMV battery failure during rail transport, providing data directly relevant to multi-modal transportation safety and policy decision-making. Recommendations on improving the passenger safety from such fire events are discussed elsewhere [19].

2 Train Stopping and Evacuation Time

The time required to evacuate a building typically requires estimation of three separate activities:

- awareness time,
- pre-travel activity time, and
- travel time.

This same approach can be applied to evacuation from a train. However, depending on the scenario, the time required to stop the train may also need to be considered.

2.1 Awareness time

Awareness time is measured from ignition until occupants become aware of the fire. For occupants in close proximity to the fire, awareness may result from environmental cues such as sounds, smells, smoke, and/or flames. Occupants outside the area of origin are likely to be unaware of the fire until alerted by other occupants or by some form of detection and/or alarm system. In the case of a LiB undergoing thermal runaway, the awareness time is typically very short, often a matter of seconds, for occupants in close proximity to the fire. Other passengers who are not immediately aware of the fire will likely soon be alerted by the commotion resulting from the rapid production and ignition of LiB battery gases.

2.2 Pre-travel activity time

Pre-travel activity time includes decision-making, locating and assisting family members, gathering belongings, and any other activities that occur before movement begins. In the case of a LiB undergoing thermal runaway, pre-travel activity time would also likely be very short for occupants in close proximity to the fire because of the obvious threat posed by the LiB fire. Other passengers in the railcar of origin are also likely to react quickly once they become aware of the fire. Passengers in other railcars may exhibit more typical occupant behavior if they become aware of the threat only through an alarm or from other passengers.

2.3 Travel time

In buildings, travel time can include both walking time and time spent queuing to move through a door or other flow-constricting obstacle. In the case of a train, occupants can be expected to move from their seats to the egress door and may have to descend stairs

if egress is not onto a level platform or adjacent railcar and passengers must instead evacuate to a right-of-way (ROW). The evacuation time for a passenger railcar has not been well studied. The most relevant study for seated passenger trains were conducted by the John A. Volpe National Transportation Systems Center (Volpe Center), in cooperation with the Massachusetts Bay Transportation Authority (MBTA) [20]. In that work, an MBTA commuter railcar carrying 84 volunteer passengers was evacuated to a level platform, which is expected to provide a comparable time scale for egress to an adjacent railcar. The measured evacuation time was 1 min and 41 s. This time should be considered optimistic because it did not account for:

- time to become aware of the fire,
- time to make decisions,
- time to locate and assist family members,
- time to gather personal belongings,
- pre-movement or pre-travel activity time,
- time to open an unfamiliar door,
- time to move through the passage between railcars,
- congestion effects in the adjacent railcar that restrict aisle movement, and
- reduced walking speed due to declining visibility in smoky conditions.

If passengers cannot evacuate to an adjacent railcar or platform but instead must exit to the ROW, evacuation can take substantially longer. In the Volpe Center study [20], an evacuation to the ROW was conducted using 15 volunteers. When scaled to 84 passengers, the reported time was 4 min and 14 s, excluding pre-movement time and the time required to stop the train.

2.4 Time required to stop a train

The evacuation of a moving train must also consider the time required to stop the train. Train stopping times are not well documented in the public domain. Minimum stopping times can be estimated using the kinematic equations of linear motion under constant acceleration as a first-order approximation [21]. Equation 1 relates the square of the final velocity (V_f) to the square of the initial velocity (V_i), the acceleration (a), and distance (x):

$$V_\mathrm{f}^2 = V_\mathrm{i}^2 + 2ax \tag{1}$$

Equation 2 relates distance required to change from V_i to V_f over a given time interval (t):

$$x = 0.5\,(V_\mathrm{i} + V_\mathrm{f})\,t \tag{2}$$

Substituting Eq. 2 into Eq. 1 gives Equation 3 that provides the time required to change velocity from V_i to V_f under constant acceleration:

$$t = \frac{V_\mathrm{f}^2 - V_\mathrm{i}^2}{a\,(V_\mathrm{i} - V_\mathrm{f})} \tag{3}$$

Here, V_i is the maximum train speed and $V_\mathrm{f} = 0$ for a complete stop. We treat a as the signed longitudinal acceleration, which is negative during braking. With $V_\mathrm{f} = 0$, Eq. 3 simplifies to Eq. 4, where t_s is the time required to stop the train:

$$t_\mathrm{s} = \frac{-V_\mathrm{i}}{a} \tag{4}$$

To bound the stopping time, we compiled maximum potential operating speeds and reported service and emergency deceleration rates from publicly available specifications for passenger rail systems worldwide. Table 1 summarizes exemplar values for passenger rail systems worldwide. Columns 1–2 list the country and city/system. Column 3 provides the maximum operating speed. Columns 4–5 list service and emergency decelerations. Columns 6–7 report minimum stopping times computed from Eq. 4, assuming the train is traveling at maximum speed and decelerates at the service or emergency rate (depending on the values found in the literature). Column 8 provides the corresponding source. The bottom two rows report the minimum and maximum values observed across the systems. These values are consistent with passenger stability research, suggesting a maximum tolerable longitudinal deceleration of approximately 1.3 m/s^2 for unsupported standing passengers and about 2.5 m/s^2 as a limit at which seated passengers may begin to lose stability [22].

Table 1 Summary of minimum theoretical stop times based only on the kinematic equations.

Country	**City/System**	**Max Speed (km/h)**	**Service Decel. (m/s^2)**	**Emergency Decel. (m/s^2)**	**Service Stop Time** (s)	**Emergency Stop Time** (s)	**Source**
France	Paris RER A	120	1.15	1.25	29	27	[23]
France	SNCF Transilien	140	1.05	—	37	—	[24]
Germany	S-Bahn (Berlin)	100	1.3	—	21	—	[25]
Germany	DB Regio (S-Bahns)	140	0.9	—	43	—	[26]
Germany	DB Regio (various)	160	0.9	—	49	—	[27]
Germany	Hamburg S-Bahn	100	0.7	1.2	40	23	[28]
Hong Kong	Airport Express	135	1.1	1.35	34	28	[29]
Japan	Tokyo Metro	120	1.11	1.25	30	27	[30]
Japan	Keikyu (multiple)	120	1.11	1.25	30	27	[31]
Netherlands	NS – Sprinter	160	1.1	—	40	—	[32]
South Korea	Seoul Metro Line 2	110	0.97	1.25	31	24	[33]
UK	London Underground	100	1.15	1.4	24	20	[34]
USA	New York Subway	80	1.3	1.4	19	18	[35]
USA	Philadelphia–SEPTA	160	1.12	1.33	34	38	[36]
	Minimum	80	0.7	1.2	19	18	
	Maximum	160	1.3	1.4	43	28	

The total time required to stop a passenger train will be longer than the minimum values in Table 1. Additional time components may include:

1. time for passengers, crew, or onboard detection systems to recognize an EMV failure or fire,
2. time for crew to reach the affected railcar if they are not already present,
3. time to communicate with the train operator,
4. operator reaction and decision making time before initiating braking, and
5. braking system response time before full braking force is achieved.

3 Experimental Setup

3.1 Railcar Description

The experiments were conducted in a single-level intercity passenger railcar representative of a coach designed in the late 1970s and still in widespread service following mid-life refurbishment. The railcar interior was configured with 72 upholstered passenger seats, a wheelchair space, overhead luggage racks, exit doors at both ends and sides of the railcar, and end-door connections to adjacent railcars. Figure 1 shows the floor plan along with the main features of the railcar. The overall dimensions of the railcar were 26.0 m (85 ft 4 in) in length, 3.2 m (10 ft 6 in) in width, and 3.9 m (12 ft 8 in) in height. The finished floor level was 1.33 m (52.25 in) above ground/track level. Figure 2 is an exterior photograph of the railcar showing the egress doors and instrumentation routed through multiple windows. Although the underlying railcar structure reflects its original design era, the seat cushions and upholstery had been replaced several times, most recently during an interior refurbishment circa 2017–2018. Figure 3 shows the interior seating configuration and overhead storage area; the photo was taken from the end of the railcar opposite the fire area of origin.

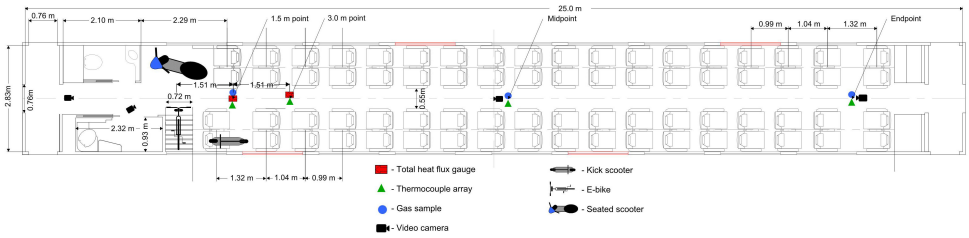


Fig. 1 Floor plan of the intercity railcar showing main features, instrumentation layout, and EMV locations used in these experiments.

3.2 EMV Description and Locations

The EMVs used in these experiments were chosen to cover a broad spectrum of vehicles that could reasonably be expected to be brought onboard an intercity railcar. Figure 4 shows the three different vehicle types in situ just prior to each experiment. EMV placement in each experiment followed common practice and was selected to represent likely onboard storage locations for each vehicle type. Because the railcar was used for four experiments with the same general area of origin, the ceiling directly above the EMV, and approximately 1 m in all directions, was protected with ceramic fiber blanket and cementitious fiberboard. The protected walls and ceiling can be seen in Figure 4.



Fig. 2 Exterior photograph of the intercity railcar after the experiments, with instrumentation lines still in place.



Fig. 3 Interior photograph showing the seating configuration and overhead storage area.

The standing e-scooter was the smallest of the three vehicles, with the lowest capacity battery and smallest tires, representing the lowest fuel load of the three vehicles. Such a device, with the handlebar folded down, can be placed in an overhead rack and could also potentially fit under seats. The e-bike was hung by the rear wheel on a hook included in the convertible luggage rack adjacent to the toilet. The front wheel was removed, consistent with the instructions included in the rack. The hook is visible on the right side of Figure 4. The seated e-scooter was positioned in the wheelchair space at the end of the railcar, see Figure 1. There is no designated area for seated e-scooters, so this device was placed in the only location that could accommodate it while maintaining a clear aisle.



Fig. 4 Electric micromobility vehicles (EMVs) in situ prior to ignition. The wall and ceiling protection, consisting of ceramic fiber blanket and cementitious fiberboard, is visible in the photos.

3.3 Battery Pack Configuration

The battery packs from the EMVs used in this study were assembled from multiple 18650-format lithium-ion cells [37] wired in both series (S) and parallel (P) [38]. The number of cells in series determines the pack voltage, and the number of cells in parallel determines the capacity and current capability. Each EMV had a different battery pack configuration considered representative of the EMV configurations evaluated in this study. The standing e-scooter was equipped with a 13S4P pack, the e-bike used a 13S8P configuration, and the seated e-scooter used a higher voltage 17S8P pack. Accordingly, the 13S packs operated at a nominal voltage of approximately 46.8 V, while the 17S pack operated at approximately 61–63 V. The corresponding pack energy contents were approximately 0.49 kWh for the standing e-scooter, 1.25 kWh for the e-bike, and 1.2–1.3 kWh for the seated e-scooter. Series and parallel counts were established from pack and BMS labeling, nominal voltage ratings, and inspection of the battery packs.

Based on the labeling on the individual 18650 cells, the standing e-scooter and e-bike employed nickel-based layered oxide lithium-ion cells, corresponding to the IEC INR chemistry class, which includes nickel–manganese–cobalt (NMC) and nickel–cobalt–aluminum (NCA) cathode systems [39]. The seated e-scooter employed ICR-type cells, indicating a cobalt-rich lithium cobalt oxide ($LiCoO_2$, LCO) chemistry [39].

3.4 Instrumentation

The railcar was instrumented to measure gas temperatures, pressure, total heat flux, and gas species concentrations. Figure 1 shows the instrumentation layout and the EMV placement locations used across the experiments. The instrumentation layout was consistent across tests, while device position varied based on the most likely storage location near the front of the railcar.

Gas temperatures were measured using 1.25 mm (0.05 in) bare-bead, Inconel-sheathed Chromel–Alumel (Type K) thermocouples (TCs). Small-diameter TCs were used to reduce errors associated with radiative heating and cooling. The total expanded uncertainty in temperature measurements was estimated as ±15%, consistent with prior work [40, 41]. Thermocouple arrays were installed at specified locations along the railcar, as shown in Figure 1. Each array consisted of eight TCs, with the uppermost TC positioned 25 mm (1 in) below the ceiling and the remaining seven TCs spaced at 0.305 m (1 ft) intervals.

Four total heat flux gauges were installed near the fire along the railcar aisle at the 1.5 m and 3.0 m stations (see Figure 1). Two gauges were installed at each station at heights of 0.91 m and 1.51 m above the floor and oriented horizontally in the plane of the aisle. Total heat flux was measured using water-cooled Schmidt–Boelter gauges. An international round-robin study indicates a typical Schmidt–Boelter uncertainty of ±8% [42].

Six gas sampling ports were installed at three distances along the aisle: near the device, near the midpoint of the railcar, and near the opposite end (see Figure 1. At each distance, ports were installed at 0.91 m (3 ft) and 1.51 m (5 ft) above the floor (see Figure 1). Gas samples were analyzed using oxygen (paramagnetic alternating pressure) and combined carbon monoxide/carbon dioxide (non-dispersive infrared) analyzers. The analyzer system has demonstrated a relative expanded uncertainty of approximately ±1% compared to span gas volume fractions [43]. Considering compartment non-uniformity and the limited number of sampling locations, an estimated uncertainty of ±12% was applied [44].

To minimize transport time, samples were drawn from the railcar using a vacuum/pressure diaphragm pump rated at 21 L/min (0.75 CFM). Sampling ports consisted of 9 mm (3/8 in) OD stainless steel tubing fixed to the floor. Sample gas passed through a condensate trap for moisture removal and then through 5 μm and 3 μm polyester filters located in the nearest row of seats. Downstream of the filters, the line transitioned from stainless steel to polyethylene tubing and exited the railcar through a small hole drilled in a polycarbonate window. The polyethylene tubing then ran approximately 30 m to the instrumentation trailer, where the sample entered the analyzer/pump rack. At the rack inlet, the sample passed through a 0.3 μm HEPA filter prior to the sample pump. Downstream of the pump, but upstream of the analyzers, the sample passed through a drierite filter to remove remaining moisture and then through a 0.01 μm filter. Before each experiment, the transport time from each sampling port to each analyzer was measured using a calibration gas; this time lag was applied during post-processing to synchronize gas measurements with other instrumentation.

4 Tenability Analysis

When assessing life safety hazards in fires, fire engineers typically apply three tenability criteria: visibility, toxicity, and thermal effects. Tenability was assessed using video recordings, gas temperatures, heat fluxes, and gas species measurements, including CO, CO_2, and O_2. In this section, the three tenability criteria are briefly described; additional detail is provided in the referenced literature.

4.1 Visibility

Measuring visibility directly in a fire experiment is difficult due to the harsh environment and the need to obtain measurements at multiple locations within the space. In these experiments, video recordings from cameras located approximately 1.5 m above the floor were reviewed to determine the approximate times when the ceiling jet reached the midpoint and endpoint of the railcar. The same recordings were also used to estimate the times when visibility was considered to be completely lost at the midpoint and endpoint. These observations provide a practical measure of visibility loss along the escape route, although they do not represent a direct optical-density measurement.

4.2 Toxicity

Fractional effective dose (FED) provides a cumulative metric that accounts for exposure to toxic species when assessing occupant response to toxic products in smoke. The FED accounts for the toxic effect of CO, hypoxia due to reduced oxygen (O_2), and increased respiration resulting from elevated carbon dioxide (CO_2). An occupant's FED depends on the egress route, travel speed, respiration rate, and local species concentrations along that route. The governing FED formulation was developed by Purser [45], and calculation procedures are described in the SFPE Handbook of Fire Protection Engineering [46] and ISO 13571 [47].

Fire toxicity depends strongly on fuel chemistry and ventilation conditions. In most enclosure fires, the primary cause of fatal and incapacitating injury is inhalation of toxic gases rather than direct flame contact. Carbon monoxide (CO) is widely recognized as the dominant toxicant in enclosure fires and the primary contributor to smoke toxicity, as evidenced by carboxyhemoglobin levels reported in fire fatalities [48–51]. CO is generated in nearly all fires due to incomplete combustion and is typically present at high concentrations, particularly under ventilation-limited conditions. Hydrogen cyanide (HCN), produced when nitrogen-containing fuels are involved in a fire, is substantially more toxic per unit concentration than CO. Nitrogen-rich materials such as polyurethane foams, wool, and certain synthetic polymers are common sources of HCN in fires.

Experimental studies, particularly those conducted by NIST, have demonstrated significant HCN production from polyurethane foams under realistic fire conditions. Studies of lithium-ion battery fires indicate that HCN is typically present in low or inconsistent concentrations relative to CO [52, 53]. It is expected that significant quantities of HCN can be produced in this and similar railcars, due to the heavy use of plastic seating and surface finishes, and that HCN may contribute significantly to

increasing the FED. However, HCN was not included in the FED calculations for two reasons: 1) because a field-deployable continuous HCN measurement system suitable for these experiments was not available, and 2) because it is anticipated that significant HCN production would not occur until after the involvement of railcar seat materials, which was demonstrated to begin after the period of interest studied in the following analysis.

When interpreting the value of the FED, a log-normal distribution with a standard deviation of 1 is commonly used to represent population susceptibility [47]. An FED = 1 is often interpreted as fatal to approximately 50% of the population; FED = 2 corresponds to approximately 76%; FED = 0.3, a common design criterion, corresponds to approximately 11%; and FED = 0.1 corresponds to approximately 1%.

4.3 Thermal

To assess incapacitation due to thermal exposure during egress, the thermal fractional effective dose (FED-T) is used. FED-T is a cumulative measure of thermal exposure from radiant and convective heat. A value of zero indicates negligible thermal injury; FED-T = 1 is often interpreted as incapacitating 50% of the population. For design purposes, FED-T = 0.3 is commonly adopted. The FED-T calculation in this paper follows ISO 13571 [47] and procedures described in the SFPE Handbook [46].

FED-T was evaluated at 1 s resolution using the measured gas temperature (T) and radiant heat flux (q_{rad}) when $q_{\mathrm{rad}} > 2.5$ kW/m^2. In locations where heat flux was not directly measured, such as the midpoint and endpoint of the railcar, q_{rad} from the smoke layer was estimated following the SFPE Handbook [46]:

$$q_{\mathrm{rad}} = \varepsilon\sigma \left(T_{\mathrm{smoke}}^4 - T_{\mathrm{skin}}^4\right) \tag{5}$$

where T_{smoke} was estimated using the TC temperature at 2.1 m height, T_{skin} was assumed to be 311 K, ε was assumed to be 0.5, and σ is the Stefan–Boltzmann constant (5.67×10^{-11} kW/m^2 K^4).

5 Results

Raw measurement data for these experiments has been documented and collated, and is hosted for free, available upon request.

5.1 Standing e-scooter in overhead rack

For the standing e-scooter experiment, the handlebar was folded down and the standing e-scooter was placed in the overhead rack at the front of the passenger railcar. This position was considered a likely storage location for this type of device. Figure 5 shows the standing e-scooter in the overhead rack with the ceiling protection in place. Also visible are the first thermocouple (TC) array and two heat flux gauge towers.

Multiple video cameras were installed inside the railcar. Post-processing of the videos indicates that the time between first visible battery gas release and ignition of the battery gas cloud was 7 s. The release of battery gas was the first visual indicator of thermal runaway that could be observed by passengers. Figure 6 shows a sequence

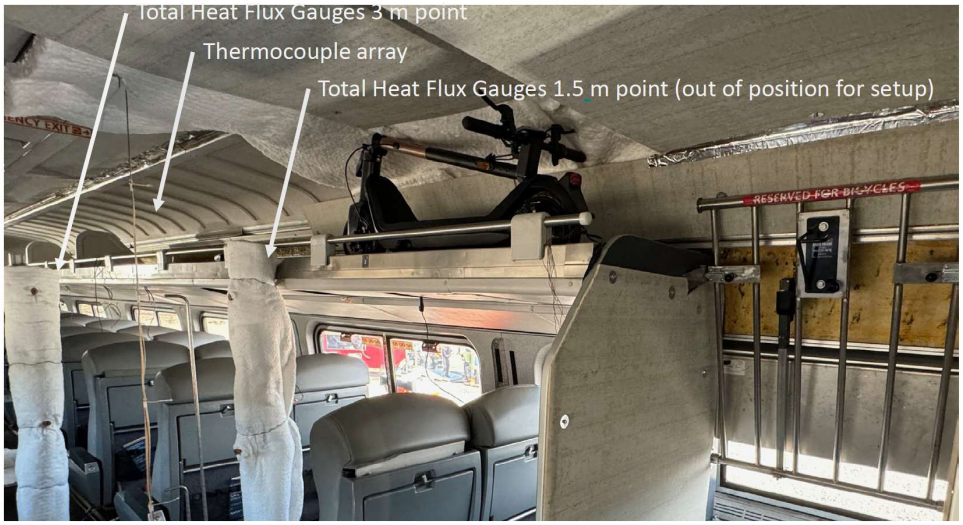


Fig. 5 Photograph of the standing e-scooter installed in the overhead rack with ceramic fiber blanket and cementitious fiberboard installed on the ceiling and upper wall.

of nine video images starting 1 s before ignition of the battery gas cloud. The time since first visible gas release is shown in the lower-right corner of each image, with ignition occurring at $t = 7$ s. The first image ($t = 6$ s) shows the gas cloud immediately prior to ignition. The remaining images show flames extending along the ceiling, away from the e-scooter. The 7 s delay between visible gas release and ignition provides nearby occupants with limited time to recognize and respond to the hazard. Firefighters entered the railcar from the fire end of the railcar to extinguish the fire and applied water 253 s after battery gas was first ejected from the e-scooter.

Figure 7 shows the time history of the average temperature computed from the top three TCs (upper layer) and the bottom three TCs (lower layer) at each of four TC arrays along the main aisle. Occupants are unlikely to be aware of an overheating battery pack (or any other unprovoked mechanism of thermal runaway initiation) until battery gases become visible. The overheating process was initiated 820 s before battery gas was first visibly discharged from the e-scooter, and no visual or audible indications occurred prior to the gas release. Accordingly, in Figure 7 and all other time-history plots, the time axis is shifted such that $t = 0$ s corresponds to the first visible battery gas release. Figure 7 also highlights key event timings: battery gas release, gas ignition, smoke observed at the midpoint, smoke observed at the endpoint, complete loss of visibility at the midpoint, and complete loss of visibility at the endpoint.

The TC array closest to the e-scooter was located at the 1.5 m station, adjacent to the front wheel. As shown in Figure 7, the average upper-layer temperature at this location was substantially higher than at other locations. Immediately after ignition,



Fig. 6 Video sequence from the standing e-scooter experiment. The sequence starts 1 s before ignition of the battery gas cloud. Images are shown at 1 s intervals; $t = 0$ s corresponds to first visible battery gas release, and ignition occurs at $t = 7$ s.

the average upper-layer temperature exceeded 300°C and then decreased to approximately 250°C until water was applied. The average upper-layer temperature at 1.5 m was strongly influenced by the uppermost TC, located 25 mm below the ceiling, which intermittently measured 500–600°C due to flame contact. The next two TCs were below 200°C approximately 5 s after ignition.

At the 3.0 m station, approximately 1.5 m from the e-scooter, temperatures were much lower, peaking near 160°C at ignition before dropping below 100°C. At the midpoint, the average upper-layer temperature remained below 70°C, and at the endpoint it remained below 50°C. Lower-layer temperatures at all locations remained below 50°C; at the midpoint and endpoint they were near ambient for the duration of the experiment. Between 170 and 195 s, an electrical fault caused by battery short circuiting interfered with millivolt TC signals, producing unrealistic readings. Data in that interval were treated as unreliable and have been removed from the plot.

Figure 8 shows FED at the gas sampling locations along the escape route: the 1.5 m station, midpoint, and endpoint. At each location, measurements were obtained at 0.91 m and 1.5 m above the floor. For the standing e-scooter experiment, FED > 0.3 occurred only at the endpoint over the 420 s interval shown. At the 1.5 m station and midpoint, FED < 0.15. At the endpoint, FED > 0.3 occurred 278 s after first visible battery gas release at 1.5 m height and 403 s after first visible battery gas release at 0.91 m height.

The FED exceeded the 0.3 threshold only at the endpoint, furthest from the fire, because of the elevated location of the standing e-scooter in the overhead rack and the resulting smoke transport pattern. With the fire located near the ceiling, entrainment

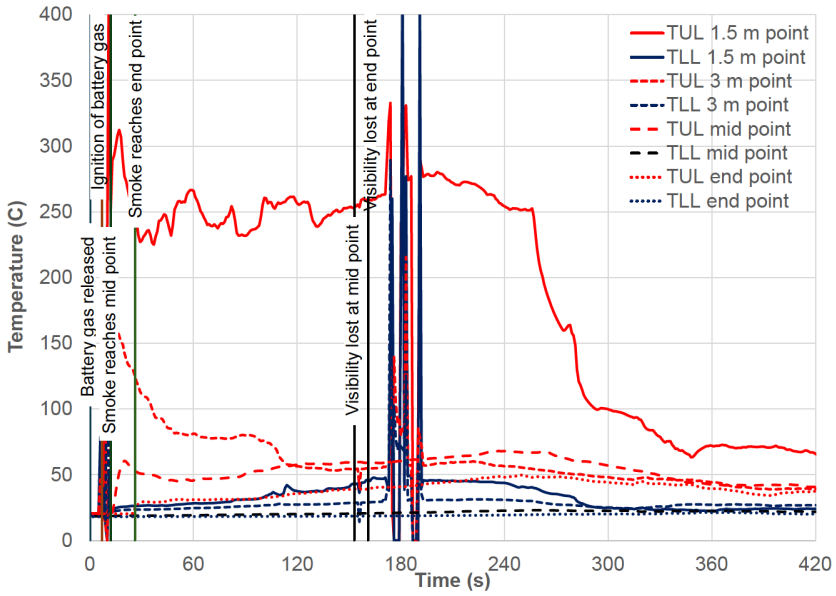


Fig. 7 Standing e-scooter average temperature for the three highest TCs (upper layer) and three lowest TCs (lower layer) on TC arrays installed along the escape route from the fire area to the exit door at the far end of the railcar.

into the plume was reduced compared with a fire located near floor level. As a result, the initial ceiling jet remained above the 0.91 m and 1.5 m gas sampling locations as the smoke traveled down the railcar. The smoke reached the endpoint first as the ceiling jet, which impinged on the end wall forming a wall jet before being redirected back toward the sampling probes. Consequently, the cumulative FED was highest at the endpoint sampling locations, even though these locations were furthest from the fire.

Figure 9 shows the FED-T history for the standing e-scooter experiment at the height/location combinations evaluated along the escape route. Values are computed at 0.91 m and 1.5 m above the floor to represent crouching and standing occupants. As noted above, data between 170 and 195 s were unreliable due to TC signal interference. Because FED-T is cumulative, it is not reported beyond 170 s for this experiment.

After ignition (t = 7 s), FED-T near the fire at the 1.5 m and 3.0 m stations, at 1.5 m height, increased rapidly due to exposure to the initial fireball (see Fig. 6). By 17 s, FED-T $>$ 0.3 at the 3.0 m station, and by 59 s, FED-T $>$ 0.3 at the 1.5 m station. At other measurement locations, FED-T did not exceed 0.3 during the reported interval.

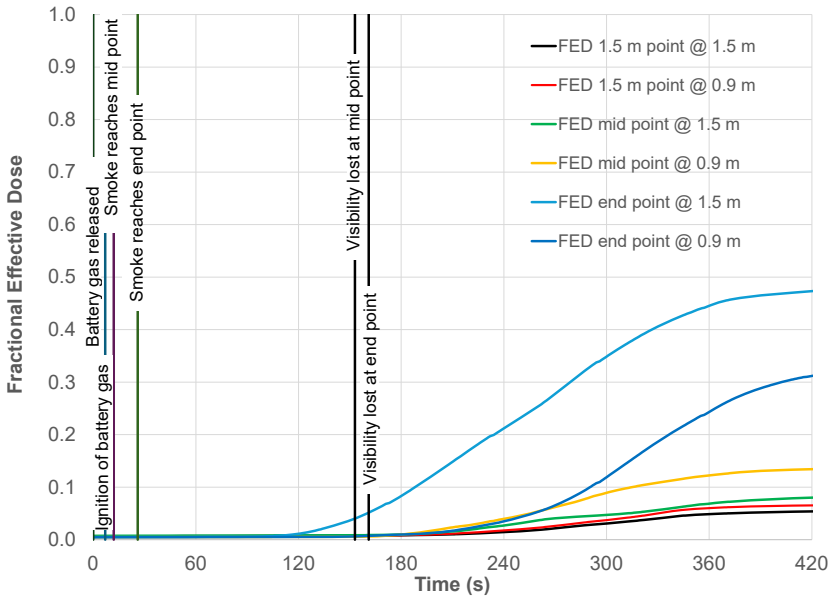


Fig. 8 Standing e-scooter fractional effective dose for gas sampling locations along the escape route from the fire area to the exit door at the opposite end of the railcar.

At the 1.5 m and 3.0 m stations, the dominant contribution to FED-T was radiant exposure measured by the heat flux gauges rather than convective exposure inferred from temperature. FED-T exceeded the 0.3 threshold only at the 1.5 m and 3.0 m stations. At 1.5 m height, FED-T increased sharply after ignition due to the intense flame from the e-scooter, indicating that occupants in close proximity to the e-scooter would be exposed to an immediate thermal hazard. Because heat flux gauges measure directional flux, the measured radiant exposure depends on gauge orientation. In these experiments, the gauges were oriented along the aisle rather than facing directly toward the fire. As a result, the calculated FED-T near the fire likely underestimate the thermal exposure that would be experienced by an occupant facing the e-scooter.

Table 2 summarizes key event times for each experiment, with $t = 0$ s defined as the first visible battery gas release. The table reports the delay to ignition of the battery gas cloud, the time for smoke to reach the midpoint and endpoint of the railcar, the time to complete loss of visibility at the midpoint and endpoint, and the times at which asphyxiant tenability was compromised (FED > 0.3) in the area of origin, midpoint, and endpoint. FED threshold-crossing times are reported at 1.5 m and 0.91 m above the floor. The ignition time is the delay between first visible battery

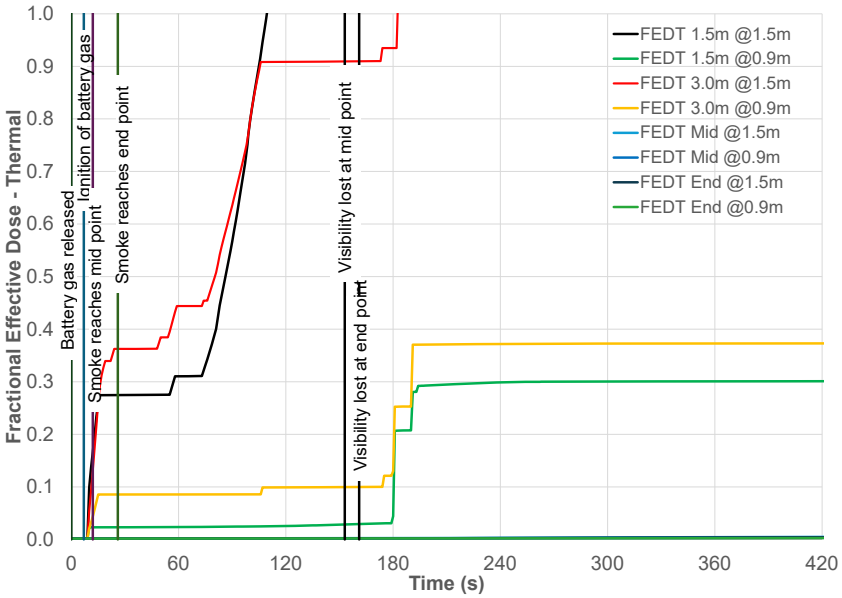


Fig. 9 Standing e-scooter experiment thermal fractional effective dose (FED-T) computed from TC arrays and heat flux gauges along the escape route from the fire area to the exit door at the opposite end of the railcar.

gas release and ignition of the battery gas cloud. The time to complete loss of visibility along the railcar was determined from video observations. In all experiments, visibility loss occurred before the FED criterion was reached at locations remote from the fire.

Table 2 Summary of the time from first visible battery gas release to ignition, complete loss of visibility, and FED threshold crossing at measurement locations along the escape route. Times are in seconds. Area of origin is abbreviated as "AoO"

Experimental Vehicle	**Ignition of battery gas**	**Smoke reaches midpoint of railcar**	**Smoke reaches endpoint of railcar**	**Complete loss of visibility midpoint of railcar**	**Complete loss of visibility endpoint of railcar**	**Asphyxiant tenability compromised at AoO (1.5/0.91 m)**	**Asphyxiant tenability compromised at midpoint (1.5/0.91 m)**	**Asphyxiant tenability compromised at endpoint (1.5/0.91 m)**
Standing e-scooter	7	12	26	153	161	NR	NR	278/403
E-bike	1	10	28	110	231	557/520	445/546	428/586
Seated e-scooter 1	90	95	109	182	199	163/342	262/365	307/394
Seated e-scooter 2	27	38	61	204	273	337/*	327/383	343/402

FED threshold-crossing times are based on the full available gas-analyzer record, which may extend beyond the 420 s interval shown in the plots.
NR = Not reached.
*Data between 170 and 195 s were unreliable due to TC signal interference and are not reported.

5.2 E-bike in luggage rack

For the e-bike experiment, the bike was placed in the luggage rack at the front of the passenger railcar. Figure 10 shows the e-bike hanging in the converted luggage rack with cementitious fiberboard added to protect the walls of the luggage area visible to the left of the e-bike.



Fig. 10 Photograph of the e-bike hanging in the converted luggage rack with ceramic fiber blanket and cementitious fiberboard installed on the ceiling and upper walls, and cementitious fiberboard installed on the luggage rack walls.

Figure 11 shows a sequence of nine video images starting 1 s before ignition of the battery gas cloud. Video post-processing indicates that the delay between first visible battery gas release and ignition was approximately 1 s. This rapid transition from gas release to ignition provides occupants near the e-bike essentially no time to recognize and respond to the hazard. Firefighters entered the railcar from the fire end to extinguish the fire and applied water 740 s after first visible battery gas release from the bike battery.



Fig. 11 Video sequence from the e-bike experiment starting 1 s before ignition of the battery gases. Images are shown at 1 s intervals; $t = 0$ s corresponds to first visible battery gas release, and ignition occurs at approximately $t = 1$ s.

Figure 12 shows the average upper-layer temperature, computed from the top three TCs, and lower-layer temperature, computed from the bottom three TCs, at each of four TC arrays along the main aisle. Overheating was initiated 1430 s before battery gas was first visible. Here again, $t = 0$ s corresponds to the first visible battery gas release. The TC array closest to the bike was located at the 1.5 m station, approximately 1.5 m from the hanging bike. At the 1.5 m and 3.0 m stations, oscillations in the temperature signal were observed as the fire intensity varied during thermal runaway propagation through the battery pack. The maximum average upper-layer temperature was 180°C at the 1.5 m station. At the midpoint and endpoint, average upper- and lower-layer temperatures remained below 30°C.

Figure 13 shows FED computed for each gas sampling location along the escape route. Over the 420 s interval shown, FED > 0.3 did not occur at any monitoring location. The maximum FED during this interval occurred at the endpoint at 1.5 m above the floor. As shown in Table 2, FED > 0.3 was reached later in the full gas-analyzer record, with the earliest threshold crossing occurring at the endpoint, 1.5 m above the floor, at 428 s. Visibility at the endpoint was lost at 231 s, well before the asphyxiant FED threshold was reached.

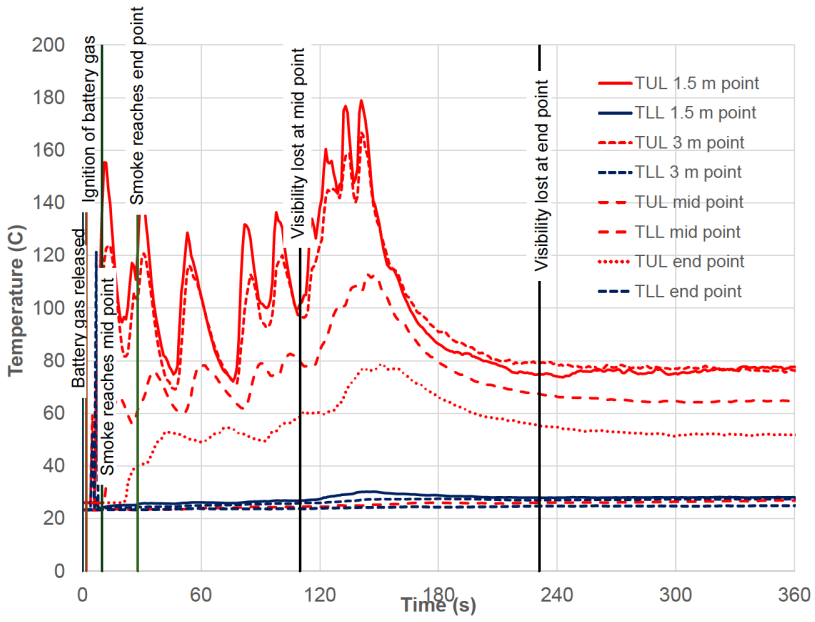


Fig. 12 E-bike experiment average temperature for the three highest TCs (upper layer) and three lowest TCs (lower layer) on TC arrays installed along the escape route from the fire area to the exit door at the opposite end of the railcar.

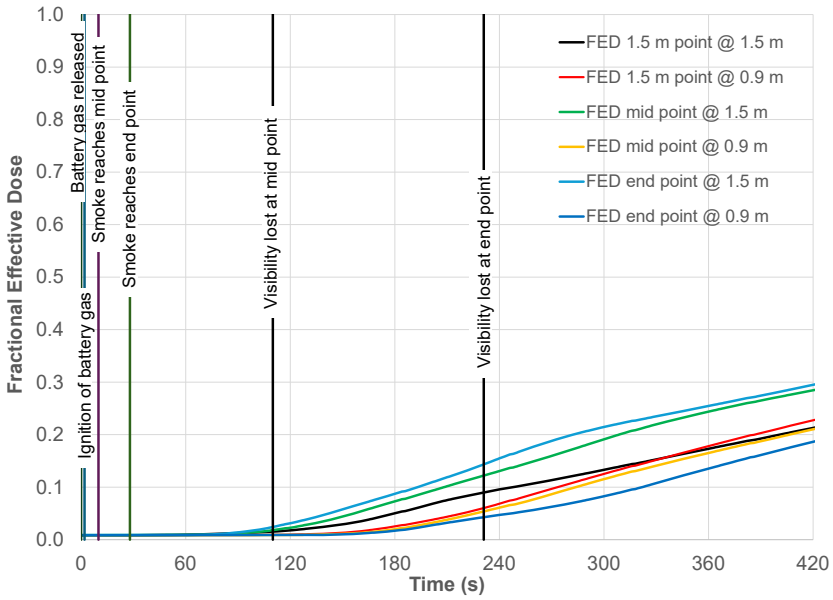


Fig. 13 E-bike fractional effective dose for gas sampling locations along the escape route from the fire area to the exit door at the opposite end of the railcar.

The calculated FED-T history is shown in Figure 14. Because of the separation distance between the bike and the nearest TC array, as well as shielding provided by the solid luggage rack wall, FED-T did not exceed 0.05 over the interval shown, well below the 0.3 threshold. However, occupants seated across the aisle from the luggage rack could have experienced greater thermal exposure than indicated by the aisle-oriented instrumentation.

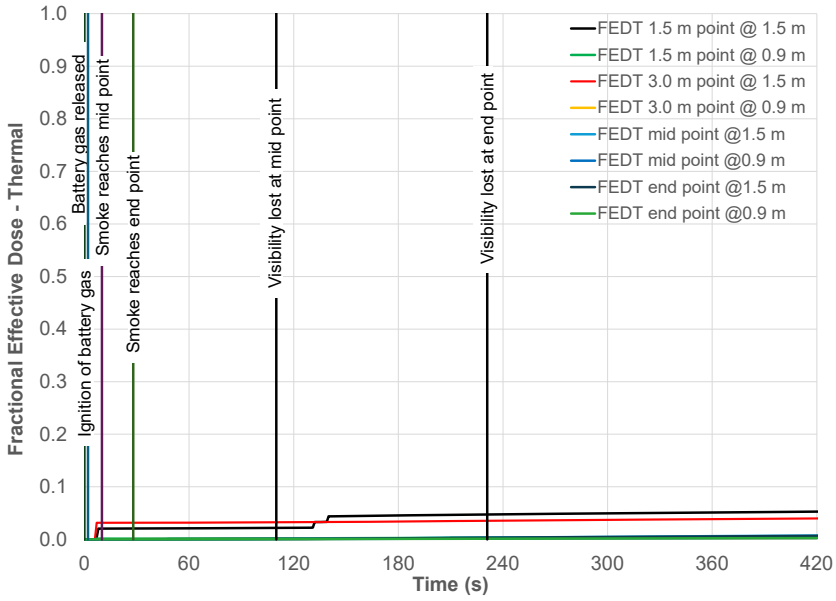


Fig. 14 E-bike experiment thermal fractional effective dose (FED-T) computed from TC arrays along the escape route from the fire area to the exit door at the opposite end of the railcar.

5.3 Seated e-scooter 1 in wheelchair space

For the first seated e-scooter experiment (seated e-scooter 1), the vehicle was located in the wheelchair space at the front of the passenger railcar. This area is the open space between the accessible restroom and the first two seats. Figure 15 shows seated e-scooter 1 positioned in the space, leaving no legroom for a passenger seated in the adjacent seats. Adjacent wall linings were also protected. No protection was installed over the fixed passenger seats.



Fig. 15 Photograph of the first seated e-scooter placed in the wheelchair space with ceramic fiber blanket protecting the overhead plastic, cementitious fiberboard installed on the walls, and unprotected passenger seats adjacent to the e-scooter.

Figure 16 shows a sequence of nine video images starting 1 s before ignition of the battery gas cloud. Post-processing of the videos indicates that the time delay between first visible battery gas release and ignition was 90 s. The time from first visible gas release is shown in the lower-right corner of each image; ignition occurs at $t = 90$ s.

Figure 17 shows the average upper-layer temperature, computed from the top three TCs, and lower-layer temperature, computed from the bottom three TCs, at each of four TC arrays along the escape route. Overheating was initiated 775 s before battery gas was first visible. In Figure 17 and all other time-history plots in this subsection, $t = 0$ s corresponds to the first visible battery gas release. The TC array closest to seated e-scooter 1 was located at the 1.5 m station, approximately 1.5 m from the e-scooter center. The average upper-layer temperatures followed similar trends across arrays. After the initial fireball, temperatures plateaued while burning remained largely confined to the e-scooter. After approximately 240 s, the fire spread to nearby



Fig. 16 Video sequence for seated e-scooter experiment 1 starting 1 s before ignition of the battery gas cloud. Images are shown at 1 s intervals; $t = 0$ s corresponds to first visible battery gas release, and ignition at $t = 90$ s.

seats, increasing the heat release rate and producing a peak temperature above 650°C at approximately 345 s.

Figure 18 shows FED calculated for each gas sampling location along the escape route. All reported sampling points exceeded FED = 0.3 within the 420 s interval shown. At each distance, the 1.5 m-high sampling location exceeded FED = 0.3 earlier than the corresponding 0.91 m-high location, demonstrating stratification of toxic products within the railcar. As shown in Table 2, FED > 0.3 was reached first at 1.5 m above the floor in the area of origin at 163 s, followed by the midpoint at 262 s and the endpoint at 307 s. Visibility was completely lost at the midpoint at 182 s and at the endpoint at 199 s, before the asphyxiant FED threshold was reached at those remote locations. Thus, for seated e-scooter 1, loss of visibility would impair egress before FED-based asphyxiant tenability was compromised at the midpoint and endpoint.

The calculated FED-T history is shown in Figure 19. The time axis starts at $t = 0$ s, when battery gas was first visible. Because of the separation distance between the e-scooter and the closest TC array, and shielding provided by passenger seats, FED-T remained low for the first 115 s. A brief flare produced a spike in the nearest heat flux gauge, resulting in a measurable contribution to FED-T at the 1.5 m station, 1.5 m above the floor. FED-T then plateaued until approximately 257 s, when nearby seats became involved and FED-T increased rapidly at the 1.5 m and 3.0 m stations. At approximately 280 s, FED-T at the 1.5 m station exceeded 0.3; among the locations that exceeded this threshold, the last crossing occurred at approximately 340 s. At the midpoint and endpoint, FED-T < 0.1 over the 420 s interval shown.

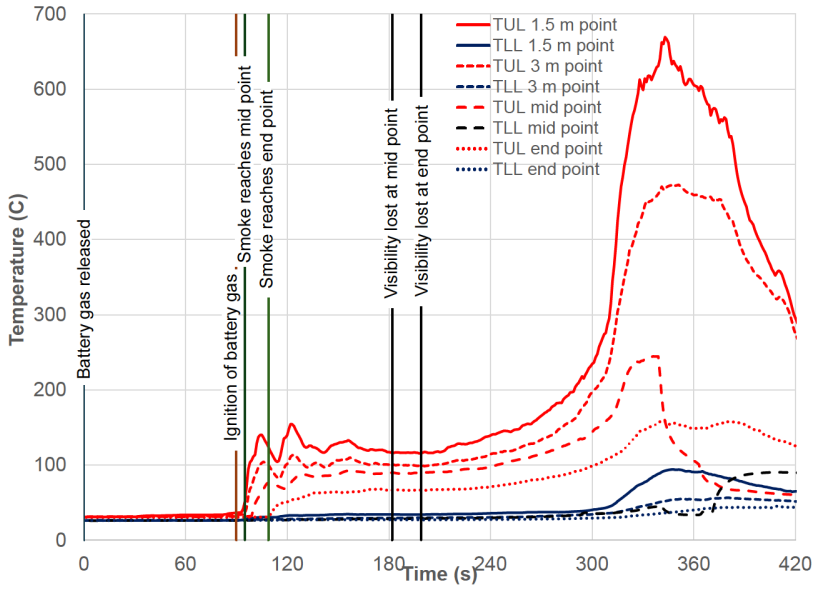


Fig. 17 Seated e-scooter experiment 1 average temperature for the three highest TCs (upper layer) and three lowest TCs (lower layer) on TC arrays installed along the escape route from the AoO to the exit door at the opposite end of the railcar.

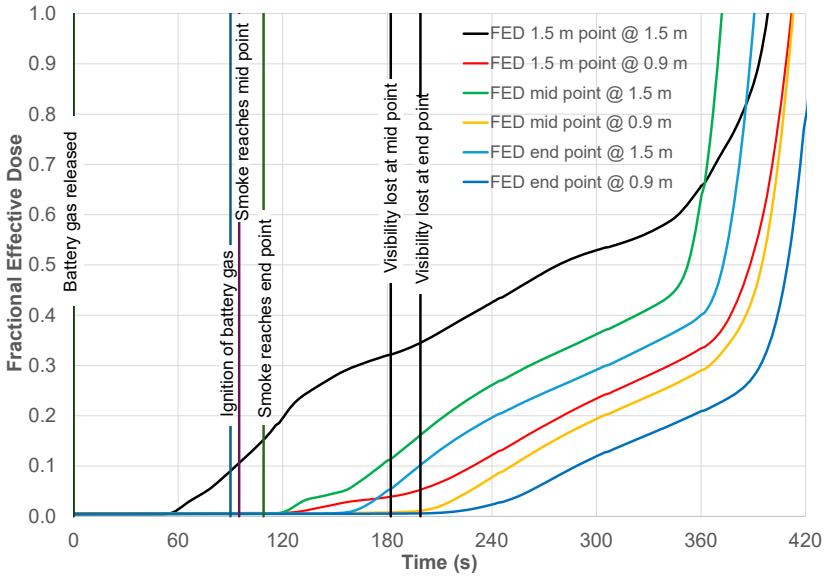


Fig. 18 Seated e-scooter experiment 1 fractional effective dose (FED) at gas sampling locations along the escape route from the fire area to the exit door at the opposite end of the railcar.

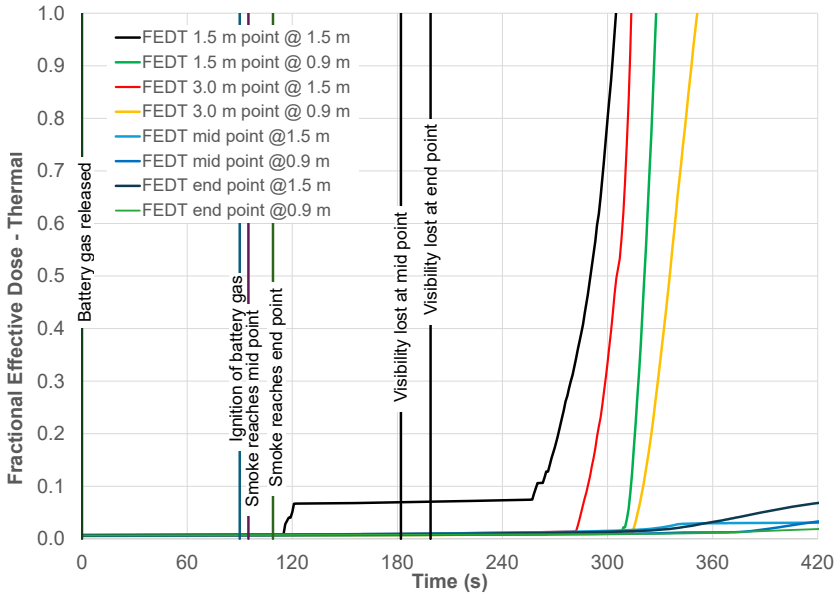


Fig. 19 Seated e-scooter experiment 1 thermal fractional effective dose (FED-T) computed from TC arrays along the escape route from the fire area to the exit door at the opposite end of the railcar.

5.4 Seated e-scooter 2 in wheelchair space

For the second seated e-scooter experiment (seated e-scooter 2), the vehicle was also located in the wheelchair space at the front of the passenger railcar. Figure 20 shows seated e-scooter 2 positioned in the damaged area from the prior experiment. The two adjacent seat cushions and back cushions were replaced for this experiment. The inner polycarbonate window pane behind the e-scooter had begun to melt and slump away from the outer pane; the outer pane remained intact.



Fig. 20 Photograph of seated e-scooter experiment 2 placed in the wheelchair space. Damage to the area of origin from seated e-scooter experiment 1 can be seen behind the vehicle. Seat and back cushions in the adjacent row were replaced before this experiment.

Figure 21 shows a sequence of nine video images starting 1 s before ignition of the battery gas cloud. Video post-processing indicates that the delay between first visible battery gas release and ignition was 27 s. For this experiment, ignition was triggered using an electric match. The first image is 1 s before ignition and shows the battery gas cloud around the e-scooter. Firefighters entered the railcar from the fire end to extinguish the fire and applied water 576 s after first visible battery gas release from the e-scooter.

Figure 22 shows the average upper-layer and lower-layer temperatures along the main aisle for seated e-scooter experiment 2. Overheating was initiated 576 s before battery gas was first visible. As above, $t = 0$ s corresponds to the first visible battery gas release. The TC array closest to seated e-scooter 2 was at the 1.5 m station, approximately 1.5 m from the e-scooter center. After the initial fireball, temperatures



Fig. 21 Video sequence for seated e-scooter experiment 2 starting 1 s before ignition of the battery gases. Images are shown at 1 s intervals; $t = 0$ s corresponds to first visible battery gas release, and ignition occurs at $t = 27$ s.

plateaued while burning remained largely confined to the e-scooter. After approximately 180 s, the fire spread to nearby seats, increasing the heat release rate and producing a peak temperature above 700°C at approximately 390 s.

Figure 23 shows FED at the gas sampling locations along the escape route for seated e-scooter experiment 2. All reported sampling points exceeded FED = 0.3 within the 420 s interval shown. As in seated e-scooter experiment 1, the 1.5 m-high sampling points exceeded FED = 0.3 earlier than the corresponding 0.91 m-high points, indicating stratification of toxic products within the railcar. As shown in Table 2, the earliest reported FED > 0.3 threshold crossing occurred at 327 s at the midpoint, 1.5 m above the floor, while the area-of-origin 0.91 m value was not reported because the corresponding gas analyzer was not operating correctly.

The calculated FED-T history for seated e-scooter experiment 2 is shown in Figure 24. The time axis starts at $t = 0$ s, when battery gas was first visible. Because of the separation distance between the e-scooter and the closest TC array, and shielding provided by passenger seats, FED-T remained small for the first 190 s. FED-T then increased rapidly at the 1.5 m and 3.0 m stations. At approximately 200 s, FED-T at the 1.5 m station exceeded 0.3; among the locations that exceeded this threshold, the last crossing occurred at approximately 340 s. At the midpoint and endpoint, FED-T < 0.3 over the 420 s interval shown.

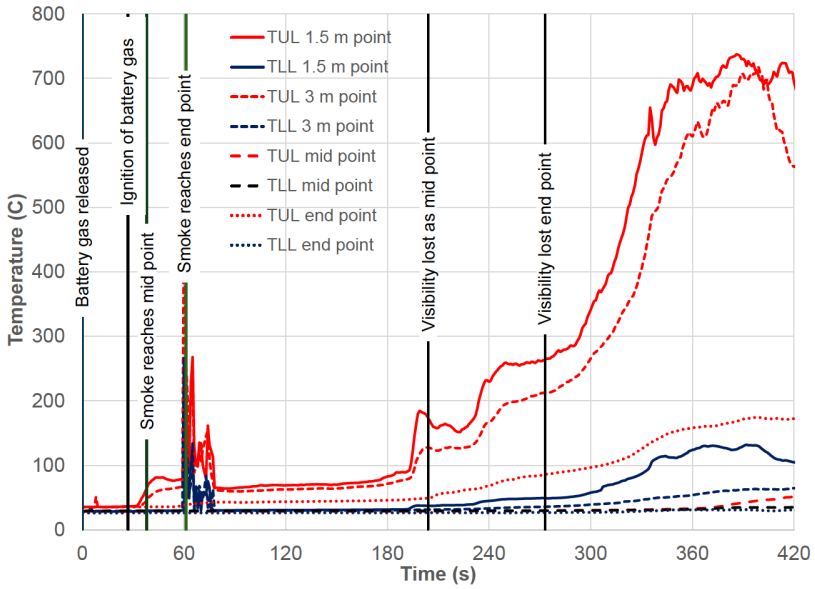


Fig. 22 Seated e-scooter experiment 2 average temperature for the three highest TCs (upper layer) and three lowest TCs (lower layer) on TC arrays installed along the escape route from the area of origin to the exit door at the opposite end of the railcar.

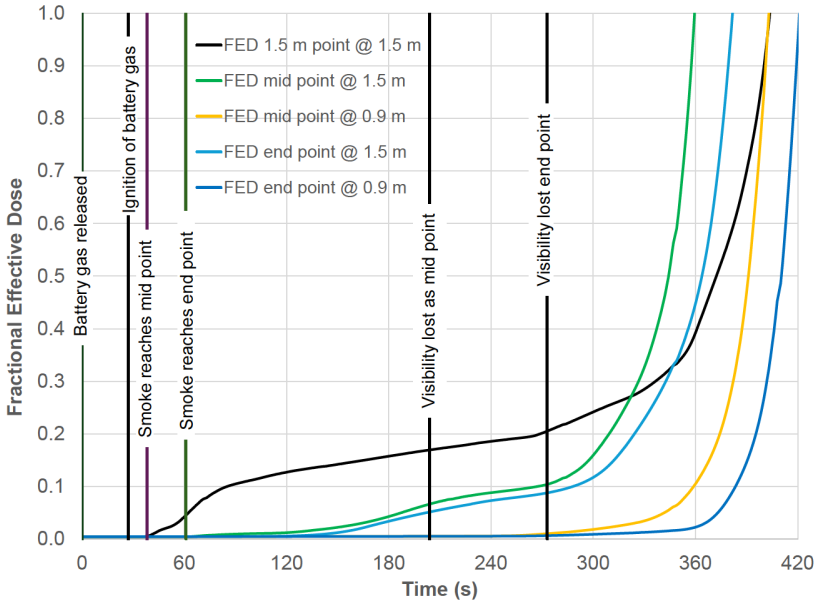


Fig. 23 Seated e-scooter experiment 2 fractional effective dose (FED) at gas sampling locations along the escape route from the area of origin to the exit door at the opposite end of the railcar.

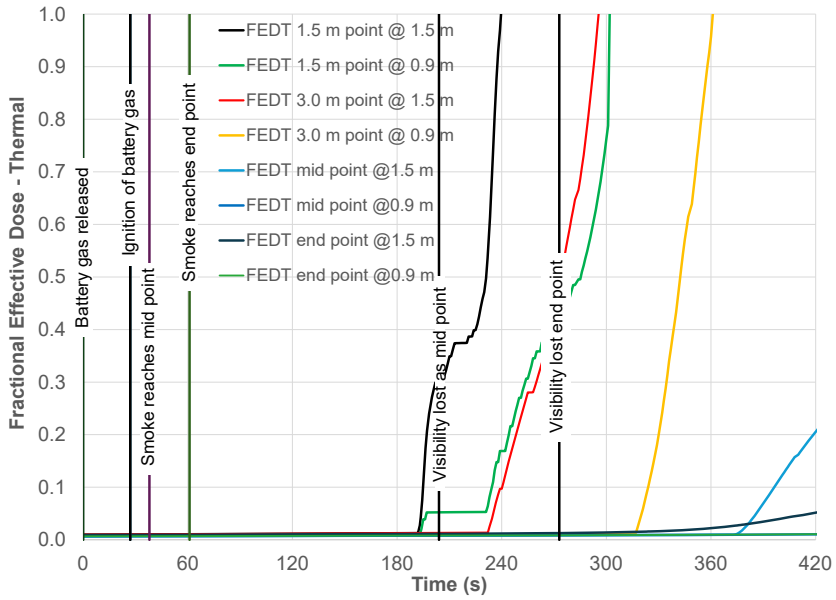


Fig. 24 Seated e-scooter experiment 2 thermal fractional effective dose (FED-T) computed from TC arrays along the escape route from the area of origin to the exit door at the opposite end of the railcar.

6 Conclusions

Based on the results presented here and prior work [17, 54], occupants are unlikely to be aware of a battery pack undergoing thermal runaway until battery gases become visible. The time between visible gas release and ignition may be so short that occupants in close proximity to the EMV could be exposed to severe thermal conditions from the ensuing fireball. In these experiments, visibility was lost before the fractional effective dose (FED) exceeded the 0.3 threshold at several locations along the escape route. Reduced visibility can have significant psychological and physical effects and is expected to slow evacuation.

The literature review of evacuation and train stopping time indicates that stopping a train may take more than 120 s. After the train stops, evacuation to an adjacent car or platform may optimistically require more than 100 s, while evacuation to the right-of-way may exceed 250 s. Considering additional complicating factors, including detection, communication, pre-movement, reduced visibility, and congestion, total evacuation could reasonably extend to several minutes and, in some scenarios, approach 5–10 min after an EMV failure or fire is first observed.

Based on video and post-fire observations, typical fire-retardant materials used in passenger railcars were not sufficient to prevent melting and ignition under EMV fire exposures. Rapidly developing and intense EMV fires heated plastic finish panels well ahead of visible flames, leading to melting, dripping, and ignition of ceiling and wall linings. Li-ion cells undergoing thermal runaway expelled embers and hot or molten material that attacked upholstered seating and would be expected to challenge fire-retardant treatments, increasing the likelihood of fire spread.

A primary limitation of these experiments was control of the combustible load within the car. Although seats and surface linings are fire-retardant treated, they can burn when exposed to a sufficiently large ignition source. The electric vehicles used in these experiments were capable of overcoming fire-retardant treatments and promoting fire spread over interior finishes, most notably in the second seated e-scooter test, where the fire was allowed more time to spread within the car.

The omission of HCN from the FED calculations does not change the primary finding of these experiments. In each experiment, the toxic threat from the EMV fire was demonstrated by the FED calculations before seats or other combustible materials in the railcar became a significant fuel source. Polyurethane foam is commonly used as padding in transport seating and may produce HCN when seats or other nitrogen-containing fuels become involved in the fire. However, the results indicate that an EMV fire in a passenger railcar can become a threat to occupants before other fuels in the train are substantially involved.

References

[1] Puspitasari, E., Yuen, C.W., Ibrahim, M.R.: The research landscape of first- and last-mile in public transport systems: A bibliometric analysis. KSCE Journal of Civil Engineering (2025) https://doi.org/10.1016/j.kscej.2025.100159 . Provisional DOI; final metadata (volume/issue/pages) pending

[2] Olabi, A.G., Wilberforce, T., Obaideen, K., Sayed, E.T., Shehata, N., Alami, A.H., Abdelkareem, M.A.: Micromobility: Progress, benefits, challenges, policy and regulations, energy sources and storage, and its role in achieving sustainable development goals. International Journal of Thermofluids **17**, 100292 (2023) https://doi.org/10.1016/j.ijft.2023.100292

[3] Bugryniec, P.J., Resendiz, E.G., Nwophoke, S.M., Khanna, S., James, C., Brown, S.F.: Review of gas emissions from lithium-ion battery thermal runaway failure—considering toxic and flammable compounds. Journal of Energy Storage **87**, 111288 (2024) https://doi.org/10.1016/j.est.2024.111288

[4] Wang, Q., Mao, B., Stoliarov, S.I., Sun, J.: A review of lithium ion battery failure mechanisms and fire prevention strategies. Progress in Energy and Combustion Science **73**, 95–131 (2019) https://doi.org/10.1016/j.pecs.2019.03.002

[5] Zhang, G., Wei, X., Chen, S., Zhu, J., Han, G., Dai, H.: Revealing the impact of slight electrical abuse on the thermal safety characteristics for lithium-ion batteries. ACS Applied Energy Materials **4**, 12858–12870 (2021) https://doi.org/10.1021/acsaem.1c02537

[6] Jeon, M., Lee, E., Park, H., Yoon, H., Keel, S.: Effect of thermal abuse conditions on thermal runaway of NCA 18650 cylindrical lithium-ion battery. Batteries **8**(10), 196 (2022) https://doi.org/10.3390/batteries8100196

[7] Sun, P., Huang, X., Bisschop, R., Niu, H.: A review of battery fires in electric vehicles. Fire Technology **56**, 1361–1410 (2020) https://doi.org/10.1007/s10694-019-00944-3

[8] Liu, B., Jia, Y., Yuan, C., Wang, L., Gao, X., Yin, S., Xu, J.: Safety issues and mechanisms of lithium-ion battery cell upon mechanical abusive loading: A review. Energy Storage Materials **24**, 85–112 (2020) https://doi.org/10.1016/j.ensm.2019.06.036

[9] Liu, B., Yin, S., Xu, J.: Integrated computation model of lithium-ion battery subject to nail penetration. Applied Energy **183**, 278–289 (2016) https://doi.org/10.1016/j.apenergy.2016.08.101

[10] Lan, T.: A critical case report of samsung note 7 recall. Frontiers in Art Research **5**(11), 1–8 (2023) https://doi.org/10.25236/FAR.2023.051101 . Francis Academic Press

[11] U.S. Department of Transportation: DOT Bans All Samsung Galaxy Note7 Phones from Airplanes. https://www.transportation.gov/briefing-room/dot-bans-all-samsung-galaxy-note7-phones-airplanes. Accessed 2024-08-21 (2016)

[12] BBC London: E-bike and e-scooter fires at record high in London. https://www.

bbc.com/news/uk-england-london-66672360. Accessed 2025-02-11 (2023)

[13] Molina, K.: E-bike, scooter fires in Ottawa prompt warnings about safety. https://www.cbc.ca/news/canada/ottawa/ebike-fire-increasing-battery-safety-advice-tips-1.6703146. CBC News. Accessed 2023-02-11 (2023)

[14] Shine, R.: Concerns over growing number of fires linked to lithium-ion batteries in e-scooters and e-bikes. https://www.abc.net.au/news/2023-01-18/e-scooter-lithium-battery-fire-risk-fears-/101863902. ABC News (Australia). Accessed 2025-02-11 (2023)

[15] Yang, L.: Deadly fire sparks scrutiny of e-bike hazards. https://www.chinadaily.com.cn/a/202402/26/WS65dbcd44a31082fc043b8f7f.html. China Daily Global. Accessed 2025-02-11 (2024)

[16] Hu, W.: How E-Bike Battery Fires Became a Deadly Crisis in New York City. https://www.nytimes.com/2023/06/21/nyregion/e-bike-lithium-battery-fires-nyc.html. The New York Times. Accessed 2025-02-11 (2023)

[17] Fleischmann, C., Weinschenk, C., Madrzykowski, D., Schraiber, A., Gaudet, B.: Quantifying the fire hazard from li-ion battery fires caused by thermal runaway in e-scooters. Fire Technology **61**, 2865–2887 (2025) https://doi.org/10.1007/s10694-025-01707-z

[18] Federal Railroad Administration: 49 CFR Part 238—Passenger Equipment Safety Standards. Code of Federal Regulations, Title 49, Part 238. U.S. Department of Transportation, Federal Railroad Administration (2026). https://www.ecfr.gov/current/title-49/subtitle-B/chapter-II/part-238

[19] Barowy, A., Fleischmann, C.: Recommendations to improve passenger railcar safety during electric micromobility vehicle fires. Technical report, Fire Safety Research Institute (May 2026). https://doi.org/10.60752/102376.32136697 . https://doi.org/10.60752/102376.32136697

[20] Markos, S.H., Pollard, J.K.: Passenger train emergency systems: Single-level commuter rail car egress experiments. Final Report DOT/FRA/ORD-15/04, U.S. Department of Transportation, Federal Railroad Administration, Office of Research and Development, Washington, DC (April 2015). Prepared by the John A. Volpe National Transportation Systems Center; also published as DOT-VNTSC-FRA-12-05

[21] Ling, S.J., Sanny, J., Moebs, W.: University Physics, Volume 1. OpenStax, Rice University, Houston, TX (2016). See Section 3.4, “Motion with Constant Acceleration”

[22] Powell, J.P., Palacín, R.: Passenger stability within moving railway vehicles: Limits on maximum longitudinal acceleration. Urban Rail Transit **1**(2), 95–103 (2015) https://doi.org/10.1007/s40864-015-0012-y

[23] Wikipedia contributors: MI 09 (RER A) — Wikipedia. https://en.wikipedia.org/wiki/MI_09. Accessed 2026-01-15 (2026)

[24] Wikipedia contributors: SNCF Class Z 50000 (Francilien) — Wikipedia. https://en.wikipedia.org/wiki/SNCF_Class_Z_50000. Accessed 2026-01-15 (2026)

[25] Wikipedia contributors: DBAG Class 481 — Wikipedia. https://en.wikipedia.org/wiki/DBAG_Class_481. Accessed 2026-01-15 (2026)

[26] Wikipedia-Autoren: DB-Baureihe 423 — Wikipedia (de). https://de.wikipedia.org/wiki/DB-Baureihe_423. German. Accessed 2026-01-15 (2026)

[27] loco-info.com editors: Bombardier Talent 2 (DB Class 442/443) — loco-info.com. https://de.wikipedia.org/wiki/Bombardier_Talent_2. Accessed 2026-01-19. Mentions braking deceleration capability with magnetic rail brakes (2025)

[28] Wikipedia-Autoren: DB-Baureihe 474 — Wikipedia (de). https://de.wikipedia.org/wiki/DB-Baureihe_474. German. Accessed 2026-01-15 (2026)

[29] Academic Dictionaries and Encyclopedias: MTR A-Stock EMU — Encyclopedia/Academic resource. https://en-academic.com/dic.nsf/enwiki/8937172. Accessed 2026-01-15. Lists acceleration and service/emergency deceleration values for AEL/TCL stock (2026)

[30] Wikipedia contributors: E231 series — Wikipedia. https://en.wikipedia.org/wiki/E231_series. Accessed 2026-01-15 (2026)

[31] Wikipedia contributors: Keikyu N1000 series — Wikipedia. https://en.wikipedia.org/wiki/Keikyu_N1000_series. Accessed 2026-01-15 (2026)

[32] Wikipedia contributors: Sprinter New Generation (SNG) — Wikipedia. https://en.wikipedia.org/wiki/Sprinter_New_Generation. Accessed 2026-01-15 (2026)

[33] Wikipedia contributors: Seoul Metro 2000 series (first generation) — Wikipedia. https://en.wikipedia.org/wiki/Seoul_Metro_2000_series_(first_generation). Accessed 2026-01-15 (2026)

[34] Wikipedia contributors: London Underground S7 and S8 Stock — Wikipedia. https://en.wikipedia.org/wiki/London_Underground_S7_and_S8_Stock. Accessed 2026-01-15 (2026)

[35] Wikipedia contributors: R211 (New York City Subway car) — Wikipedia. https://en.wikipedia.org/wiki/R211_(New_York_City_Subway_car). Accessed 2026-01-15 (2026)

[36] Hyundai Rotem: Electric Multiple Unit (EMU). https://web.archive.org/web/20111007021558/http://www.hyundai-rotem.co.kr/Eng/Business/Rail/Railroad/Product/rail1_pop04.asp. Archived by the Internet Archive Wayback Machine on 7 October 2011. Accessed 25 October 2026 (2011)

[37] Battery University: BU-301a: Types of Battery Cells. Accessed April 2026. https://batteryuniversity.com/article/bu-301a-types-of-battery-cells

[38] Battery University: BU-302: Series and Parallel Battery Configurations. Accessed April 2026. https://batteryuniversity.com/article/bu-302-series-and-parallel-battery-configurations/

[39] Nitta, N., Wu, F., Lee, J.T., Yushin, G.: Li-ion battery materials: present and future. Materials Today **18**(5), 252–264 (2015) https://doi.org/10.1016/j.mattod.2014.10.040

[40] Blevins, L.G.: Behavior of bare and aspirated thermocouples in compartment fires. In: Proceedings of the 33rd National Heat Transfer Conference, Albuquerque, NM (1999). HTD99-280

[41] Pitts, W.M., Braun, E., Peacock, R.D., Mitler, H.E., Johnsson, E.L., Reneke, P.A., Blevins, L.G.: Temperature uncertainties for bare-bead and aspirated thermocouple measurements in fire environments. In: Gritzo, L.A., Alvares, N.J. (eds.) Thermal Measurements: The Foundation of Fire Standards. ASTM International, West Conshohocken, PA (2003). https://doi.org/10.1520/STP10945S

[42] Pitts, W.M., Murthy, A.V., Ris, J.L., Filtz, J.-R., Nygård, K., Smith, D., Wetterlund, I.: Round robin study of total heat flux gauge calibration at fire laboratories. Fire Safety Journal **41**(6), 459–475 (2006) https://doi.org/10.1016/j.firesaf.2006.04.004

[43] Bundy, M.F., Hamins, A.P., Johnsson, E.L., Kim, S.C., Ko, G.H., Lenhert, D.B.: Measurements of heat and combustion products in reduced-scale ventilation-limited compartment fires. Technical Report NIST Technical Note 1483, National Institute of Standards and Technology, Gaithersburg, MD (2007)

[44] Lock, A., Bundy, M., Johnsson, E.L., Hamins, A., Ko, G.H., Hwang, C., Fuss, P., Harris, R.: Experimental study of the effects of fuel type, fuel distribution, and vent size on full-scale underventilated compartment fires in an ISO 9705 room. Technical Report NIST Technical Note 1603, National Institute of Standards and Technology, Gaithersburg, MD (2008). https://doi.org/10.6028/NIST.TN.1603

[45] Purser, D.A.: Modelling toxic and physical hazard in fire. In: Grant, C.E., Pagni, P.J. (eds.) Fire Safety Science – Proceedings of the Second International Symposium, pp. 391–402. International Association for Fire Safety Science, Hemisphere Publishing (1988). Also incorporated into the SFPE Handbook of Fire Protection Engineering

[46] Purser, D.A., McAllister, J.L.: Assessment of hazards to occupants from smoke, toxic gases, and heat. In: Hurley, M.J., *et al.*(eds.) SFPE Handbook of Fire Protection Engineering, pp. 2308–2428. Springer, New York, NY (2016). https://doi.org/10.1007/978-1-4939-2565-0_63

[47] International Organization for Standardization: ISO 13571:2012(E) — Life-threatening components of fire — Guidelines for the estimation of time to compromised tenability in fires. Technical report, International Organization for Standardization (2012). Edition 2

[48] Pitts, W.M.: Toxic yield. Nist technical note, National Institute of Standards and Technology, Gaithersburg, MD (2008). https://tsapps.nist.gov/publication/get_pdf.cfm?pub_id=911816

[49] John R. Hall, J., Harwood, B.: Smoke or burns—which is deadlier? NFPA Journal **89**, 38–43 (1995)

[50] Babrauskas, V., Levin, B.C., Gann, R.G., Paabo, M., Richard H. Harris, J., Peacock, R.D., Yusa, S.: Toxic potency measurement for fire hazard analysis. Technical Report Special Publication 827, National Institute of Standards and Technology, Gaithersburg, MD (December 1991)

[51] Babrauskas, V.: The generation of co in bench-scale fire tests and the prediction for real-scale fires. Fire and Materials **19**, 205–213 (1995)

[52] Claassen, M., Bingham, B., Chow, J.C., Watson, J.G., Wang, Y., Wang, X.: Characterization of lithium-ion battery fire emissions—part 1: Chemical composition of fine particles (pm2.5). Batteries **10**(9), 301 (2024) https://doi.org/10.3390/batteries10090301

[53] Willstrand, O., Bisschop, R., Blomqvist, P., Temple, A., Andersson, J.: Toxic Gases from Electric Vehicle Fires. In: Proceedings of the Fifth International Fire in Vehicles Conference (FIVE), Borås, Sweden (2020)

[54] Madrzykowski, D., Fleischmann, C., Weinschenk, C.: Examining the impact of residential fire sprinklers on e-scooter fires initiated by thermal runaway of li-ion batteries. Fire Technology **61**, 5753–5772 (2025) https://doi.org/10.1007/s10694-025-01808-9